# nature communications



**Article** 

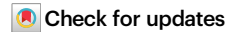
https://doi.org/10.1038/s41467-025-64772-6

# Observation of metastability in open quantum dynamics of a solid-state system

Received: 2 February 2025

Accepted: 25 September 2025

Published online: 06 November 2025



Jun-Xiang Zhang<sup>1,2,6</sup>, Yuan-De Jin  $^{3,4,6}$ , Chu-Dan Qiu $^{3,4}$ , Wen-Long Ma  $^{3,4} \boxtimes \&$  Gang-Qin Liu  $^{1,2,5} \boxtimes$ 

Metastability is a ubiquitous phenomenon in nonequilibrium physics and classical stochastic dynamics. It arises when the system dynamics settles in long-lived states before eventually decaying to true equilibria. Remarkably, it has been predicted that quantum metastability can also occur in continuousand discrete-time open quantum dynamics. However, the direct experimental observation of metastability in open quantum systems has remained elusive. Here, we experimentally observe metastability in the discrete-time evolution of a single nuclear spin in diamond, realized by sequential Ramsey interferometry measurements (RIMs) of a nearby nitrogen-vacancy electron spin. We demonstrate that the metastable polarization of the nuclear spin emerges at a metastable region of measurement times determined by the spectral structure of the quantum channel induced by the RIM. Such metastable polarization enables high-fidelity single-shot readout of the nuclear spin and the observation of an ultralong spin relaxation time of more than 10 s at room temperature. Our results represent a concrete step towards uncovering nonequilibrium physics in open quantum dynamics, which is practically relevant for the utilization of metastable information for various quantum information processing tasks.

Metastability, similar to prethermalization in nonequilibrium physics<sup>1</sup>, arises when the system relaxes into long-lived states before subsequently decaying to true stationarity much slowly. The concept of metastability is widely used, for example, in the description of the long-lived atomic state of individual atoms<sup>2</sup>, the magnetic state of single nanoparticle<sup>3</sup>, and the metastable structure and phase of condensed matter systems<sup>4,5</sup>. In these systems, metastability is mainly due to the barriers separating local minima in the energy levels of the systems.

In classical stochastic dynamics, metastability is a manifestation of a separation of time scales that arises from the splitting in the spectrum of the dynamical generator. Recently, quantum metastability theory has been extended to Markovian open quantum dynamics with a similar spectral structure in the generator<sup>6-8</sup>, where the manifold of

metastable states is argued to be composed of disjoint states, decoherence-free subspaces, and noiseless subsystems. Such metastability theory is physically interesting in its own right and stimulates the prediction of metastability phenomena in various quantum models<sup>9–17</sup>. It is also of practical importance to utilize the preserved information of quantum processes for quantum information processing<sup>18,19</sup>, especially in the presence of control imperfections or environmental noise.

For the continuous-time dynamics described by the Lindblad master equation, metastability can be observed from the distinct two-step decay of temporal correlations<sup>6</sup>. However, experimental observations remain scarce, mainly due to the difficulty in measuring temporal second- or higher-order correlations with good resolution<sup>20,21</sup>.

<sup>1</sup>Beijing National Laboratory for Condensed Matter Physics and Institute of Physics, Chinese Academy of Sciences, Beijing, China. <sup>2</sup>School of Physical Sciences, University of Chinese Academy of Sciences, Beijing, China. <sup>3</sup>State Key Laboratory of Semiconductor Physics and Chip Technologies, Institute of Semiconductors, Chinese Academy of Sciences, Beijing, China. <sup>4</sup>Center of Materials Science and Opto-Electronic Technology, University of Chinese Academy of Sciences, Beijing, China. <sup>5</sup>CAS Center of Excellence in Topological Quantum Computation, Beijing, China. <sup>6</sup>These authors contributed equally: Jun-Xiang Zhang, Yuan-De Jin. —e-mail: wenlongma@semi.ac.cn; gqliu@iphy.ac.cn

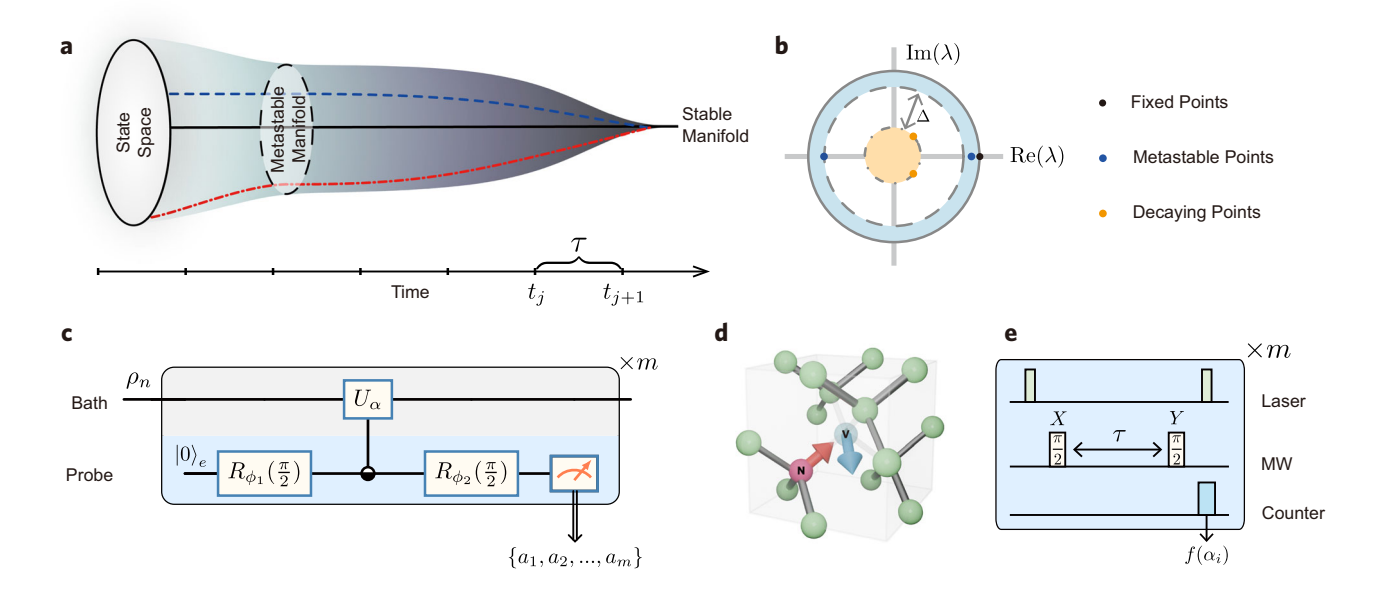


Fig. 1 | Metastability in discrete-time open quantum dynamics and its observation in diamond. a Schematic of metastability in open quantum dynamics. The states outside the metastable manifold (MM, red dot-dashed line) exhibit a two-step relaxation, i.e., first quickly relaxing into the MM and then slowly decaying into the stationary manifold (SM). The discrete-time axis implies that the open quantum dynamics is described by sequential quantum channels. b Spectrum of a quantum channel, with all eigenvalues located within the unit circle (solid circle) of the complex plane. Metastable points are located in the region with  $|\lambda| \approx 1$  (labeled with blue ring in the spectrum). The metastable region of measurement times is determined by the spectral gap  $\Delta$  between the decaying region (labeled in orange)

and the metastable region in the spectrum.  ${\bf c}$  Quantum circuit of sequential RIMs, where  $R_{\phi}(\vartheta)$  is the rotation operator of the probe qubit,  $U_{\alpha}$  is a unitary operator of the bath conditioned on the probe state  $|\alpha\rangle_e$  ( $\alpha=0,1$ ), and  $\{a_1,\ldots,a_m\}$  ( $a_i=0,1$ ) is the sequence of measurement outcomes.  ${\bf d}$  The experimental system, with the electron spin of a nitrogen-vacancy (NV) center in diamond serving as the probe qubit, and the host  $^{14}$ N nuclear spin as the quantum bath system.  ${\bf e}$  Pulse sequences to implement sequential RIMs in experiments. Laser pulses are used to polarize and read out the NV spin state, and resonant microwave (MW) pulses are used to manipulate the probe spin state.

Alternatively, certain signatures of metastability can be observed without measuring the temporal correlations (e.g., through the high-accuracy time-resolved heterodyne detection in the superconducting cavities)<sup>22</sup>; however, such approaches are often not applicable to other experimental settings.

A recent advance in quantum metastability theory is the generalization of the setting from continuous-time to discrete-time open quantum dynamics<sup>23,24</sup>. Such a framework describes the more general scenario in which each discrete evolution is induced by a quantum channel (or a completely positive and trace-preserving quantum map)<sup>25</sup>, which may not be generated by continuous-time master equations<sup>26,27</sup>. With this framework, metastable open quantum dynamics of a quantum system can be directly observed by only sequentially measuring an ancilla qubit, instead of continuously measuring the temporal correlations. Remarkably, metastability has been predicted in the commonly used Ramsey interferometry measurements (RIMs)<sup>28–30</sup>, which is easy to realize in various quantum platforms. By repeating the RIM on a probe qubit, a nearby bath system can be metastably polarized, which is manifested in statistics of the probe measurement outcomes associated with different quantum trajectories of the bath system.

Here, we report an observation of the metastable open dynamics in diamond based on sequential RIMs, using a nitrogen ( $^{14}$ N) nuclear spin as the bath system and the nitrogen-vacancy (NV) electron spin as the probe. Due to the hyperfine coupling between the bath and the probe during free evolution, each round of RIM solely applied on the probe spin induces a quantum channel on the nuclear spin, and sequential RIMs induce discrete-time open quantum dynamics on the nuclear spin (Fig. 1a). By recording the statistical results of the sequential probe measurement, we can continuously monitor the state evolution of the target spin. We directly observe the metastable polarization when varying the number of repetitions m, i.e., the bath spin is first steered to metastable (polarized) states for a finite range of

m, and eventually relaxes towards the true stable (maximally mixed) state as m continues to increase.

# **Results**

#### Metastability in sequential RIMs

We illustrate the principle of metastability by considering a typical class of sequential quantum channels on a quantum bath system, with the channel being induced by a probe qubit under a RIM sequence<sup>23</sup>. The probe qubit is coupled to the bath through the general pure-dephasing coupling

$$H = \sigma_e^z \otimes B_n + \mathbb{I}_e \otimes C_n, \tag{1}$$

where the subscripts e and n refer to the probe and bath, respectively,  $\sigma_e^i$  is the Pauli-i operator of the qubit (i=x,y,z) with  $\sigma_e^z = |0\rangle_e \langle 0| - |1\rangle_e \langle 1|$ ,  $\mathbb{I}_e$  is the identity operator of the qubit, and  $B_n(C_n)$  is the interaction (free) operator of the bath. We denote the probe qubit rotation along an axis in the equatorial plane as  $R_\phi(\vartheta) = e^{-i(\cos\phi\sigma_e^x + \sin\phi\sigma_e^y)\vartheta/2}$ , with  $\phi$  denoting the rotation axis and  $\vartheta$  the rotation angle.

For a single RIM, the probe qubit is first initialized to state  $|0\rangle_e$ , and then prepared in a superposition state  $|\psi\rangle_e = (|0\rangle_e - ie^{i\phi_1}|1\rangle_e)/\sqrt{2}$  by a rotation  $R_{\phi_1}(\frac{\pi}{2})$ . After the composite system evolving with the pure-dephasing coupling [Eq. (1)] for time  $\tau$ , the probe undergoes another rotation  $R_{\phi_2}(\frac{\pi}{2})$ , and is finally projectively measured in the basis of  $\sigma_e^z$  with the measurement outcome  $a \in \{0, 1\}$ .

The RIM sequence of the probe spin induces a quantum channel  $\phi$  on the bath,

$$\Phi(\rho_n) = \operatorname{Tr}_e \left[ U(\rho_e \otimes \rho_n) U^{\dagger} \right] = \sum_{a=0}^{\infty} M_a \rho_n M_a^{\dagger}, \tag{2}$$

where  $\rho_e = |\psi\rangle_e \langle \psi| \ (\rho_n)$  is the initial state of the probe (bath) spin,  $U = e^{-iH\tau}$  is the propagator for the composite system. By partially tracing over the probe spin, we obtain the Kraus operator  $M_a = [U_0 - (-1)^a e^{i\Delta\phi} U_1]/2$ , where  $U_\alpha = e^{-i[(-1)^a B_n + C_n]\tau}$  is a unitary operator of the bath spin conditioned on the probe spin state  $|\alpha\rangle_e \ (\alpha = 0, 1)$ , and  $\Delta\phi = \phi_1 - \phi_2$  is the phase difference between the rotation axes of two  $\pi/2$  pulses in a RIM. With the measurement outcome a, the bath state is steered to  $M_a\rho_nM_a^\dagger/p(a)$  with probability  $p(a) = {\rm Tr}\ (M_a\rho_nM_a^\dagger)$ . Note that the Kraus operators satisfy  $\sum_a M_a^\dagger M_a = \mathbb{I}_n$  with  $\mathbb{I}_n$  being the identity operator on the bath, which ensures that  $\sum_a p(a) = 1$ .

The behaviors of repetitive quantum channels can be clearly revealed by the spectral decomposition of a single channel (see "Methods"). A quantum channel has at least one fixed point (Fig. 1b), which is the state that remains unchanged after the channel <sup>31,32</sup>. It has been proved that the fixed points of the channel in Eq. (2) depend on the commutativity of  $B_n$  and  $C_n$  (see "Methods")<sup>23</sup>. If  $B_n$  commutes with  $C_n$ , i.e.,  $[B_n, C_n] = 0$ , the fixed points include the simultaneous eigenstates of  $B_n$  and  $C_n$ , then sequential RIMs of the probe spin will polarize the bath system to one of the eigenstates, also constituting a quantum non-demolition (QND) measurement on the bath spin<sup>33–38</sup>. However, if  $[B_n, C_n] \neq 0$ , the fixed points are the maximally mixed state in the whole space (or subspace) of the bath, then sequential RIMs cannot effectively measure the bath system but only perturb it.

Quantum metastability emerges when  $[B_n, C_n] \neq 0$ , but  $C_n$  is a small perturbation of  $B_n$ , then the bath will be polarized for a finite range of repetitions of RIMs. We suppose that the channel has r fixed points and q-r (q>r) metastable points, which collectively span a (q-1)-dimensional metastable manifold (MM). The region of repetition numbers for metastable polarization of the bath spin can be estimated as  $(1-|\lambda_{q+1}|)^{-1} \ll m \ll (1-|\lambda_q|)^{-1}$  when  $\lambda_q$  is very close to 1, where  $\lambda_q$  is the eigenvalue of metastable point with the smallest eigenvalue. As m increases and enters the metastable region, the bath state evolves into the MM. Beyond this region, the system further relaxes into the stationary manifold (SM), which is spanned by the fixed points. This process, during which the system first reaches the MM and then relaxes to the SM, is referred to as a two-step relaxation (see Fig. 1a).

The metastability behaviors in sequential RIMs can be directly monitored by the measurement statistics of the probe spin<sup>23</sup>. To see this, we decompose the average dynamics of sequential quantum channels into stochastic trajectories,

$$\Phi^{m}(\boldsymbol{\rho}_{n}) = \sum_{a_{1},\dots,a_{m}=0}^{1} \mathcal{M}_{a_{m}} \cdots \mathcal{M}_{a_{1}}(\boldsymbol{\rho}_{n}), \tag{3}$$

where  $\mathcal{M}_{a_i}(\cdot) = M_{a_i}(\cdot) M_{a_i}^{\dagger}$  with  $a_i \in \{0, 1\}$  being the measurement outcome of the ith RIM. For a trajectory with the sequence of measurement outcomes  $\{a_1, \ldots, a_m\}$ , the bath is steered to  $\rho'_n = \mathcal{M}_{a_m} \cdots \mathcal{M}_{a_i}(\rho_n)/p(a_1, ..., a_m)$  with probability  $p(a_1, ..., a_m) = \operatorname{Tr}[\mathcal{M}_{a_m} \cdots \mathcal{M}_{a_i}(\rho_n)]$ . With the number of outcome 0(1) in  $\{a_1, \ldots, a_m\}$  denoted as  $m_0(m_1)$  satisfying  $m_0 + m_1 = m$ , we can define the measurement polarization  $X = (m_0 - m_1)/(2m)^{23,24,39}$ , which can be used to classify different classes of stochastic trajectories that the bath system undergoes. The measurement distribution of X can show several peaks, with each peak corresponding to the quantum trajectories that lead to a fixed point (or metastable state) of the channel (see "Methods"). So in the metastable region, the distribution exhibits up to q peaks, corresponding to the metastable states. However, as m surpasses this region, the number of peaks gradually reduces to r, reflecting the final stationary states of the bath.

#### **Experimental implementation in the NV system**

We demonstrate this protocol experimentally on an NV center and a nearby <sup>14</sup>N nuclear spin in a high-purity diamond (Fig. 1d). Nuclear spins around NV centers have great potential for building quantum

networks<sup>40</sup>, storing quantum information<sup>38</sup>, performing quantum simulations<sup>41–43</sup> and sensing inertial parameters<sup>44</sup>. Access to the nuclear spins is usually based on their hyperfine interaction with the electron spin and the optical interface of the NV center. It is therefore an interesting and fundamental problem to monitor and understand the dynamics of these nuclear spins under sequential measurements acting on the central electron spin.

Specifically, an NV electron spin is a spin-1 system with a zero-field splitting D=2.87 GHz between its  $|0\rangle_e$  ( $m_s=0$ ) and  $|\pm 1\rangle_e$  ( $m_s=\pm 1$ ) state. In our experiment, a moderate external magnetic field of  $B=108.4\pm0.2$  G is applied along the NV symmetry axis (z axis) to lift the degeneracy of the  $|\pm 1\rangle_e$  states and we work in the  $\{|0\rangle_e, |-1\rangle_e\}$  subspace. The Hamiltonian in Eq. (1) becomes (in the rotating frame)

$$H = A_{zz}S_zI_z + QI_z^2 - \gamma_n \mathbf{B} \cdot \mathbf{I} + \tilde{H}_1, \tag{4}$$

where  $\mathbf{S} = (S_x, S_y, S_z)$  is the NV electron spin-1 operator,  $\mathbf{I} = (I_x, I_y, I_z)$  is the <sup>14</sup>N nuclear spin-1 operator,  $A_{zz} = -2.16$  MHz ( $A_\perp = -2.63$  MHz) is the zz-component (transverse component) of the hyperfine tensor, Q = -4.95 MHz is the quadrupolar splitting,  $\gamma_n = 1.071$  kHz/G ( $\gamma_e = 2.802$  MHz/G) being the gyromagnetic ratio of <sup>14</sup>N nuclear spin (electron spin), and  $\tilde{H}_1 = \sum_{\alpha} |\alpha\rangle_e \langle \alpha| \otimes H_n^{\alpha}$  is a second-order perturbation term with  $H_n^{\alpha} \approx \frac{\gamma_e(2-3|\alpha|)}{2D} [-\gamma_e (B_x^2 + B_y^2) + 2A_\perp (B_x I_x + B_y I_y)]$ . To introduce a noncommutativity between  $B_n = A_{zz}I_z$  and  $C_n = QI_z^2 - \gamma_n \mathbf{B} \cdot \mathbf{I} + \tilde{H}_1$ , the external magnetic field is slightly misaligned with the NV axis, i.e., there is a small tilt angle  $\theta$  between the magnetic field and NV axis. Under this circumstance, the perturbation terms  $-\gamma_n (B_x I_x + B_y I_y)$  and  $\tilde{H}_1$  lead to the metastable polarization of <sup>14</sup>N nuclear spin.

For each RIM, the resulting quantum state of the NV spin is read out by counting its spin-dependent photon number. As shown in Fig. 1e, a 532-nm laser is used to excite the NV center, and all experiments are performed at room temperature. Due to the low photon emission rate of the NV center and the poor collection efficiency, only 0.05 photons can be detected on average in each measurement, which is not sufficient to distinguish the spin states. Fortunately, the spin relaxation time of the <sup>14</sup>N nuclear spin is very long (see "Discussion" below), and many RIMs can be performed before a state jump occurs. Therefore, to obtain a reasonable signal-to-noise ratio (SNR) and to distinguish the nuclear spin states, we simply sum up the counts of the sequential measurements. We expect that the metastable polarization is easier to observe by readout methods with higher SNR, for example, the resonant excitation of the NV electron spin at low temperature <sup>45,46</sup>.

Figure 2 presents the metastable dynamics of the target nuclear spin under sequential RIMs acting on the NV electron spin. Before the measurement, the <sup>14</sup>N nuclear spin is in the thermal state, which means that its population is evenly distributed among the set of states  $\{|0\rangle_n, |\pm 1\rangle\}_n$   $\{m_l = 0, \pm 1\}$ . For a small number of RIMs (m < 5 k), the shot noise of the photon counts exceeds the count difference of the measured states, so that no efficient signal can be detected in this range. As the number of RIMs increases (m > 5 k), the measurement results begin to concentrate on two regions, which is a clear signature of the metastable polarization of the bath spin, as can be seen in the middle slice of Fig. 2a, b. We classify the trajectories based on the average photon counts with a threshold value of 0.05. If the average photon counts are less than 0.05, it is classified as a dark state; otherwise as a bright state. The experimentally resolved bright state corresponds to the maximally mixed state of the subspace spanned by  $\{|0\rangle_n, |-1\rangle_n\}$ , i.e.,  $\rho_{\rm B}=(|0\rangle_n\langle 0|+|-1\rangle_n\langle -1|)/2$ . This bright state, together with the dark state  $\rho_D = |1\rangle_n \langle 1|$ , are the extremely metastable states (EMSs) of the one-dimensional MM spanned by the fixed point and the metastable point with higher eigenvalue, as shown in Fig. 2d. Beyond the metastable region (m > 600 k), the two peaks mentioned above gradually disappear and a single peak appears, corresponding to the stable state of the system, i.e., the maximally mixed state in the

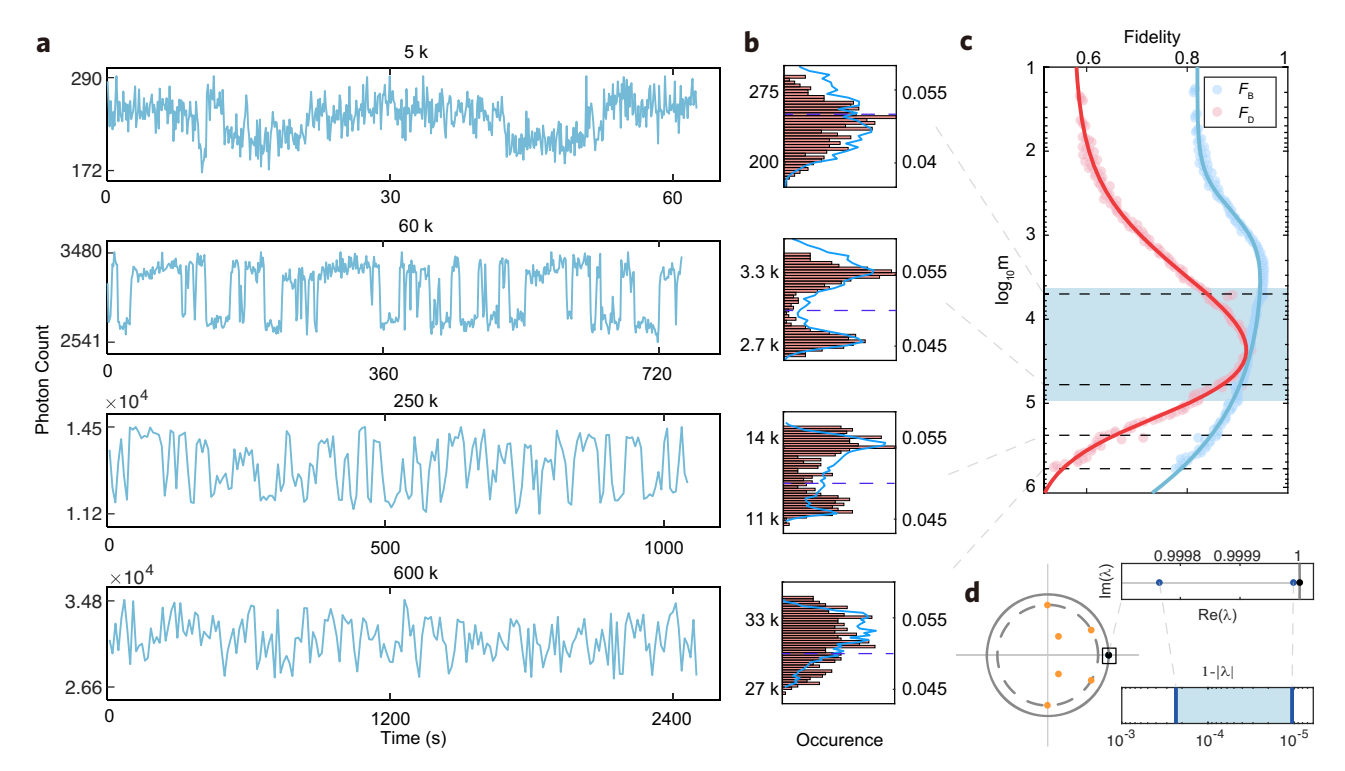


**Fig. 2** | **Metastable dynamics of a** <sup>14</sup>**N nuclear spin induced by sequential RIMs of a nearby NV electron spin. a, b** Typical PL time trace of an NV center under sequential RIMs and the corresponding distribution of the measurement results. The total and average photon counts are shown on the left and right axes, respectively. The duration of free evolution,  $\tau = 374$  ns. The number of measurement repetition m is 5 k, 60 k, 250 k, 600 k from top to bottom. When m = 5 k, it is difficult to distinguish the nuclear spin quantum states. When m = 60 k, the jump signal is concentrated in two distinct photon count intervals. As m increases further to 250 k, the overlap between the two distribution peaks becomes more pronounced. When m exceeds the metastable region, the photon counting peaks gradually merge. The blue envelopes in (**b**) indicate the normalized numerical

simulation results. **c** Numerical results. The evolution of the nuclear spin state fidelity under sequential RIMs. The initial thermal state of the nuclear spin is polarized to either the dark state  $|1\rangle_n\langle 1|$  or the bright state  $(|0\rangle_n\langle 0|+|-1\rangle_n\langle -1|)/2$ . The solid lines are fits to the simulation results. The fidelity  $F_{\rm D,B}$  quantifies how close the quantum states represented by the trajectories are to the ideal dark or bright states, respectively. **d** The channel spectrum, with one fixed point, two metastable points and six decaying points. The right pane is a magnified view of the spectrum near the metastable points, and the deviations of their eigenvalues from 1  $(1-|\lambda|)$  are shown accordingly. The metastable region and the underlying channel spectrum gap are marked with blue shades in (**c**) and (**d**), respectively. Monte Carlo simulations are conducted with a tilt angle  $\theta=8.8^{\circ}$  and 3000 samples.

whole space  $\mathbb{I}_n/3$ . More data and simulations can be found in Figs. S4–S6.

To quantitatively understand the metastable dynamics of the nuclear spin, we perform numerical simulations that take into account the parameters of hyperfine coupling, the strength and orientation of the external magnetic field, and the readout efficiency of the NV electron spin. The metastable states can be characterized by comparing them with the ideal polarized states, i.e., by the fidelity  $F_{\text{D(B)}} = F(\rho_{\text{D(B)}}, \rho'_n)$ , where  $F(\rho, \sigma) = \text{Tr} \sqrt{\rho^{1/2} \sigma \rho^{1/2}}$  and  $\rho'_n$  is the actual state. As shown in Fig. 2c, the experimentally observed metastable dynamics of the <sup>14</sup>N can be well reproduced with a tilt angle of the magnetic field of  $\theta = 8.8^{\circ}$ .

Since the <sup>14</sup>N nuclear spin is a three-level system, three-state jumps are expected in the PL time trace. The fact that only two stages appear indicates that two of them cannot be distinguished under the current experimental conditions (B = 108.4 G and  $\theta = 8.8^{\circ}$ ). Interestingly, when a smaller angle of the external magnetic field ( $\theta < 2^{\circ}$ ) is chosen, three-state jumps are observed in the experiment, as shown in Fig. 3a, b. The physical picture behind this is that the external magnetic field can influence the metastability behavior by changing the value of  $[B_n, C_n]$ . Through numerical simulations we find that under the magnetic field with  $\theta = 8.8^{\circ}$ , three peaks emerge at around 5 k measurements and two of them merge into one before 60 k measurements, so that only two-state jumps are observed in our measured region (Fig. 2a). Figure 3c shows the calculated dependence of the two-state jump and three-state jump regions as a function of the orientation of the magnetic field. For a smaller tilt angle of the external magnetic field (e.g.,  $\theta = 2^{\circ}$ ),

the metastable region of the three-state jump can survive under a large number of RIM measurements, which allows the experimental observation of the three-peak signals (see Supplementary Note II for more details).

#### Single-shot readout of a single nuclear spin

The observed metastability provides a simple and efficient way to realize high-fidelity single-shot readout of the nuclear spin. Under a magnetic field tilt angle  $\theta$  = 7°  $\pm$  2° and a RIM interval of  $\tau$  = 374 ns, the quantum jumps of the nuclear spin are clearly observed in the range of measurement numbers from 5 k to 250 k, as shown in Fig. 2a. We then characterize the readout fidelity of the nuclear spin using the method developed in ref. 36,47. By pre-selecting bright-state and dark-state photon count thresholds, we filter quantum jump signals across different measurement repetitions. This results in photon number distributions for bright and dark states with initialization fidelity higher than 99%. We then quantify the state-dependent readout fidelities, as summarized in Fig. 4a and Fig. S9b, c. It is worth noting that both the external magnetic field and the RIM interval affect the occurrence of the metastable states, so as to the optimal readout region. With a repetition number of m = 80 k (total measurement time 1.695 s), a readout fidelity of 97% ± 2% with a threshold count value of 2950 is achieved.

Next, we investigate the relaxation mechanism of the <sup>14</sup>N nuclear spin under repeated measurements. Previous studies have shown that the flip-flop process in the excited state of the NV center is the dominant factor, and usually a large external magnetic field (>2000 G) is

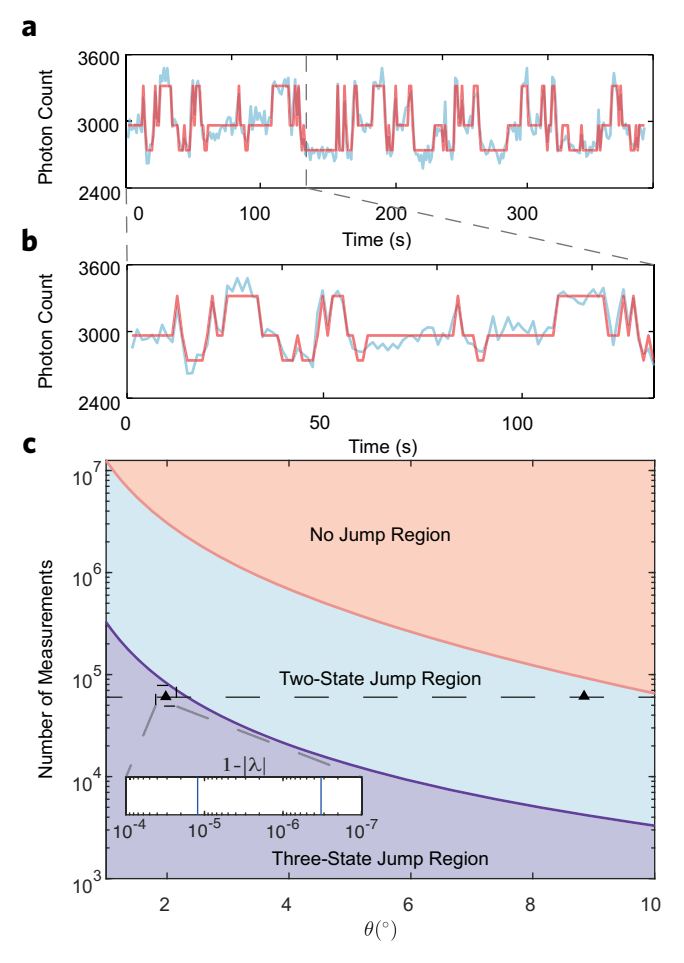


**Fig. 3** | **Magnetic field dependence of the metastable region.** a Three-state jump signal of the <sup>14</sup>N nuclear spin. The signal is observed when the magnetic field is close to the NV axis ( $\theta = 2^{\circ}$ ), with a RIM duration  $\tau = 374$  ns and the number of repetitions m = 60 k. The red fitting line is extracted from the hidden Markov model. **b** The first 100 points of of three-state jump signal. The three plateau levels correspond to the states  $|+1\rangle_n$ ,  $|0\rangle_n$ , and  $|-1\rangle_n$  of the <sup>14</sup>N nuclear spin. **c** Phase diagram for metastability. The metastable region for the number of measurements m depends on the orientation of the magnetic field. The dashed line marks the case of m = 60 k, with the two black triangles indicating experimental conditions used. The left point with  $\theta = 2^{\circ}$  gives the three-state jump signals explicitly shown in (a) and (b). The corresponding metastable region, quantified by the deviations of their eigenvalues from 1, is shown in the inset. The right point with  $\theta = 8.8^{\circ}$  corresponds to the two-state jump signal shown in Fig. 2a.

applied to suppress this term so that single-shot readout of the nuclear spin can be achieved  $^{36,37}$ . Alternatively, our results show that the nuclear spin relaxation can be largely suppressed by simply shortening the duration of the excitation laser. Moreover, by inserting additional waiting intervals between the sequential RIMs, a longer nuclear spin  $T_1$  is observed, as summarized in Fig. 4b. The longest  $T_1$  measured in our experiment is  $15 \pm 3.5$  s. To our knowledge, this is the first time that a single-shot readout of the  $^{14}$ N nuclear spin has been achieved at room temperature and under a small magnetic field.

Finally, we perform nuclear magnetic resonance (NMR) and Rabi measurements to demonstrate coherent control of the  $^{14}$ N nuclear spin. The nuclear spin state is first prepared by a RIM measurement sequence (either in the bright or dark state), then an RF pulse is applied to flip the nuclear spin, and a second RIM measurement is performed to determine the nuclear spin state. The RF pulse has either a fixed duration (30  $\mu$ s for NMR) or a fixed frequency (at the resonance frequency of NMR). The sequence is repeated 80 k times, and the probability of nuclear spin flip is recorded. Figure 4c shows the NMR signal

at 4973.0 kHz, which corresponds to the  $^{14}N$  nuclear spin being in  $|+1\rangle_n$  state. Figure 4d shows the Rabi oscillation of the  $^{14}N$  nuclear spin between the states  $|+1\rangle_n$  and  $|0\rangle_n$ . These results further confirm that the observed quantum jump signal originates from the  $^{14}N$  nuclear spin.

#### **Discussion**

In conclusion, we have directly observed metastability in the discretetime open quantum dynamics of a single nuclear spin in diamond, induced by sequential RIMs of a probe NV electron spin. The observed metastable polarization of the nuclear spin demonstrates that QND measurements of an arbitrary quantum system can be realized in a much broader range of conditions, and go far beyond the QND experiments where the ancilla and the measured system are tuned to maximally entangled states<sup>36–38</sup>. Such schemes can also be easily extended to other physical platforms, including trapped ions, superconducting circuits, and other semiconductor single-spin systems.

The framework for constructing QND measurements can be generalized to implement dynamical-decoupling-based quantum metrology in noisy environments, which enables us to learn the probebath and bath-bath coupling strengths<sup>48,49</sup>, the magnetic field<sup>46,50,51</sup> and bath spin polarization<sup>52,53</sup>. On the other hand, our results point out a potential issue in constructing quantum networks with NV centers or other single-spin systems, since sequential measurements of an ancilla can cause its nearby memory to equilibrate towards a maximally mixed state, leading to the loss of information about the stored state.

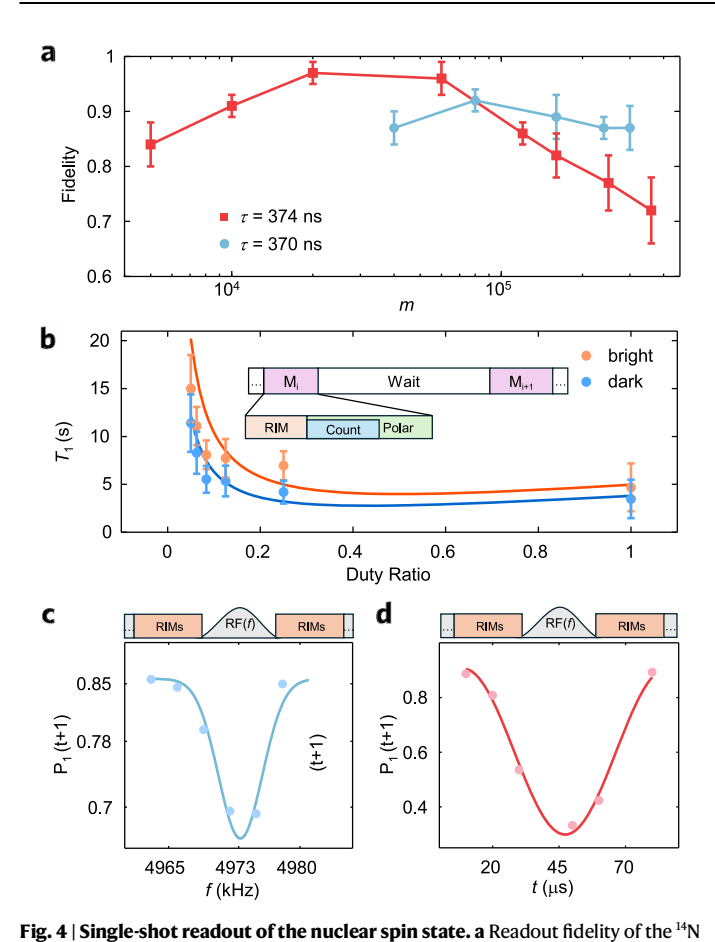
The generality of our protocols also sets a blueprint for future studies of nonequilibrium phenomena in open quantum systems. It will be interesting future work to realize more general channels in both theory and experiments, whose fixed points may include decoherence-free subspaces or noise-free subsystems, and to explore the metastability phenomena for protected coding and logical gates. Such phenomena can be directly relevant to quantum information processing, since the fixed points of a quantum channel with preserved information can become metastable when control errors or environmental noise are taken into account.

#### Methods

# **Experimental setup and sample information**

The experiments are performed with a [100]-oriented, type IIa singlecrystal diamond produced by Element Six, with a natural <sup>13</sup>C isotopic abundance of 1.1%. The NV centers used in this study are generated through electron irradiation and subsequently annealed under vacuum conditions. To improve photon collection efficiency, a solid immersion lens (SIL) is etched onto the diamond surface. Under saturation conditions, the photon counting rate of the NV center is about 300 kcps. The diamond was mounted on a custom-built confocal microscope, and a 532-nm laser was used to initialize and read out the NV spin states. The laser pulses are timing-controlled with an acoustic optical modulator (AOM, Gooch & Housego 3350-199) and focused on the diamond sample through an objective (NA = 0.9). The fluorescence emitted from the NV center is collected with the same objective, passed through a dichroic mirror and a 650-nm long-pass filter, then coupled into a multimode fiber and detected with a single photon detector (SPD). The fluorescence photons are counted with an data acquisition card (NI-6343).

To control the NV electron spin and the <sup>14</sup>N nuclear spins, we use an arbitrary waveform generator (AWG, Techtronix 5024C) to generate transistor-transistor logic (TTL) signals and low-frequency analog signals. The synchronized TTL signals are used to control the AOM, RF switches and counters. For electron spin manipulation, the microwave (MW) carrier signal from a MW source (Rohde & Schwarz SMIQ03B) is combined with two analog signals using an IQ-mixer (Marki Microwave, IQ1545LMP). An additional analog channel is used to generate the RF signal for nuclear spin manipulation. Both the MW and RF



rig. 4 | single-shot readout of the indicear spin state. a Readout indenty of the N nuclear spin as a function of the measurement repetition number. The data points with  $\theta = 7^{\circ} \pm 2^{\circ}$ ,  $\tau = 374$  ns are shown in red squares, while the data points with  $\theta = 7^{\circ} \pm 2^{\circ}$ ,  $\tau = 370$  ns are shown in blue circles. **b** <sup>14</sup>N nuclear spin relaxation time (bright state in orange and dark state in blue) as a function of the duty cycle of the excitation laser pulses. The inset illustrates the experimental pulse sequence. The duty cycle is defined as the ratio of the measurement time to the waiting time in the sequence. In (**a**) and (**b**), the vertical error bars display the statistical error (s.d.) from the fit. **c** <sup>14</sup>N nuclear spin NMR, obtained by varying the radio-frequency (RF) pulse frequency at a fixed pulse duration of 30  $\mu$ s. **d** <sup>14</sup>N nuclear spin Rabi oscillations. A resonant RF pulse of a specific length is applied between every two sequential RIMs to flip the nuclear spin between the  $|0\rangle_n$  and  $|+1\rangle_n$  states, while the electron is at the  $|0\rangle_n$  state.

signals are amplified by amplifiers (Mini Circuits, ZHL-16W-43-S+ and ZHL-32A-S+). The MW and RF signals are combined by a customer-designed duplexer (DC-200 MHz, 1200 MHz-4000 MHz) and transmitted to the NV position via a gold co-planar waveguide deposited on the diamond surface.

As can be seen in the ODMR spectrum of the NV center, there is no splitting due to hyperfine interaction with strongly coupled  $^{13}$ C nuclear spin, and a static magnetic field  $B=108.4\pm0.2$  G is applied close to the NV symmetry axis. The transition between the  $|0\rangle_e\leftrightarrow|-1\rangle_e$  NV spin states is addressed via resonant microwave pulses (at the  $m_I=0$  state of the  $^{14}$ N nuclear spin). To compensate for the temperature drift of the experimental system, we re-measured the ODMR spectra and adjusted the microwaves accordingly before each of the sequential RIMs. Figure S8b shows the free-induction decay (FID) signal of the measured NV center, which yields  $T_{2e}^*=1.15\,\mu\text{s}$ .

For the <sup>14</sup>N nuclear spin, the measurement strength oscillates as a function of the RIM duration  $\tau$ . Considering the nuclear spin relaxation and the NV electron spin dephasing time,  $\tau = 374$  ns is chosen to perform the experiments. Under these circumstances, the dynamics

induced by sequential RIMs precedes the <sup>14</sup>N nuclear spin  $T_1$  process. For each RIM, an optical pulse of 220 ns is used to read out the population of the NV electron spin. After the first measurement, the nuclear spin randomly collapses to  $|0\rangle_n$  or  $|\pm 1\rangle_n$ , and in the following measurement, it remains at the same state until a quantum jump occurs. Results with more  $\tau$  value can be found in the Supplementary Information Note III.

# Quantum channels and their representations

Quantum channel, also called completely positive and trace-preserving (CPTP) map, describes the most general (closed or open) quantum dynamics that a quantum system can undergo. Each quantum channel has four different representations: the Kraus representation, the Stinespring representation, the natural representation, and the Choi representation. The Kraus representation is the most commonly used one and characterizes a channel by a set of Kraus operators  $\{M_a\}_{a=1}^r$ , which satisfy  $\sum_{a=1}^r M_a^\dagger M_a = \mathbb{I}$ , such that  $\Phi(\cdot) = \sum_{a=1}^r M_a(\cdot) M_a^\dagger = \sum_{a=1}^r \mathcal{M}_a(\cdot)$ . The Stinespring representation is a dilation of a quantum channel, which is realized by coupling the bath system to a probe system, subjecting the composite system to a unitary evolution and then tracing over the probe system, i.e.,  $\Phi(\rho_n) = \operatorname{Tr}_e[U(\rho_e \otimes \rho_n)U^\dagger]$ , where  $\operatorname{Tr}_e[\cdot]$  denotes the partial trace over the probe qubit.

Since a quantum channel acts on the operator space of the bath system and can be considered as a superoperator, it is more convenient to use its natural representation in the Hilbert-Schmidt (HS) space. In the HS space, an operator is transformed into a vector  $(X = \sum_{i,j=1}^d x_{ij} |i\rangle \langle j| \leftrightarrow |X\rangle \rangle = \sum_{i,j=1}^d x_{ij} |ij\rangle \rangle)$ , so that each superoperator is transformed into a single matrix  $(X(\cdot)Y \to X \otimes Y^I)$ . Thus, the natural representation of  $\Phi$  is  $\hat{\Phi} = \sum_{a=1}^r \hat{\mathcal{M}}_a$  with  $\hat{\mathcal{M}}_a = M_a \otimes M_a^*$ . Note that we add hats on the operators of the HS space. In the natural representation, we can spectrally decompose the quantum channel as

$$\hat{\Phi} = \sum_{i} \lambda_{i} |R_{i}\rangle\rangle\langle\langle L_{i}|, \qquad (5)$$

where  $\lambda_i$  is the ith eigenvalue with the corresponding right (left) eigenvector  $|R_i\rangle \left\langle (|L_i\rangle \right\rangle$ ), satisfying  $\hat{\Phi}|R_i\rangle \right\rangle = \lambda_i |R_i\rangle \right\rangle$ ,  $\hat{\Phi}^\dagger |L_i\rangle \right\rangle = \lambda_i^\dagger |L_i\rangle \rangle$ , and the biorthonormalization condition  $\langle \langle L_i|R_j\rangle \rangle = {\rm Tr}(L_i^\dagger R_j) = \delta_{ij}$  with  $\delta_{ij}$  being the Kronecker delta. The eigenvalues  $\{\lambda_i\}$  of a quantum channel are all located within a unit disk of the complex plane. The eigenspaces with  $\lambda=1$  are called fixed points denoted by  $|\rho_{\rm fix}^i\rangle \rangle$ , those with  $\lambda=e^{i\phi}$  and  $\phi\neq 0$  are rotating points, and those with  $|\lambda|<1$  are decaying points that decay fast under repetitive channels since  $\hat{\Phi}^m|R_j\rangle \rangle = \lambda_j^m|R_j\rangle \rangle \to 0$  for  $|\lambda_j|<1$ .

#### Metastability in sequential quantum channels

Of particular interest are the decaying points with eigenvalue  $|\lambda_i| \approx 1$ , which are called metastable points Quantum metastability emerges when there are metastable points in the channel spectrum<sup>23</sup>. Although the information of these metastable points will be finally lost, it can be well preserved within a certain range of m. Specifically, for the channel with r fixed points and q-r metastable fixed points, the contributions of the metastable points cannot be neglected when  $m \ll \mu' = 1/|\ln |\lambda_q||$ , while the contribution of the other decaying points decays fast as m grows and can be omitted when  $m \gg \mu'' = 1/|\ln |\lambda_{q+1}||$ . So  $\mu'$  and  $\mu''$  delimit a metastable region:

$$\frac{1}{|\ln|\lambda_{q+1}||} \ll m \ll \frac{1}{|\ln|\lambda_q||}.$$
 (6)

When the eigenvalue of metastable points is very close to 1, and the decaying points relax fast, which is suitable for our case, the

metastable region can be estimated as

$$m \ll \frac{1}{|\ln |\lambda_a||} \approx \frac{1}{1 - |\lambda_a|} \tag{7}$$

In the metastable region,  $|\lambda_i|^m \approx 1$  for  $i \le q$  and  $|\lambda_j|^m \approx 0$  for j > q, then we have

$$\hat{\Phi}^{m}|\rho\rangle\rangle\simeq\sum_{i=1}^{r}c_{i}|\rho_{\text{fix}}^{i}\rangle\rangle+\sum_{i=r+1}^{q}\tilde{c}_{j}|R_{j}\rangle\rangle,$$
 (8)

for initial state  $|\rho\rangle\rangle = \sum_i c_i |R_i\rangle\rangle$  with  $\tilde{c}_j = c_j e^{im\phi_j}$ . We note that the metastable points, as well as decaying points, are trace-zero, so any metastable state in metastable manifold is a superposition of both fixed points (trace-one) and metastable points, denoted by  $\{c_1,\ldots,c_r,\tilde{c}_{r+1},\ldots,\tilde{c}_q\}$  with  $\sum_{i=1}^r c_r = 1$ , corresponding to a point in the (q-1) dimensional HS subspace.

We can transform from the HS subspace to the metastable manifold (MM), which contains the metastable states as a convex combination of q extreme metastable states (EMSs)

$$|\rho_{\rm MS}\rangle\rangle = \sum_{\nu=1}^{q} p_{\nu} |\rho_{\rm EMS}^{\nu}\rangle\rangle \tag{9}$$

with  $p_{\nu} = \langle \langle P_{\nu} | \rho_{\rm MS} \rangle \rangle$  satisfying  $\sum_{\nu} p_{\nu} = 1$ . Here,  $P_{\nu}$  is the projector to  $|\rho_{\rm EMS}^{\nu}\rangle$ , satisfying  $\langle \langle P_{\nu} | \rho_{\rm EMS}^{\mu} \rangle \rangle = \delta_{\nu\mu}$  and  $\sum_{\nu} P_{\nu} = \mathbb{I}$ . For the case of r=1 and q=2, i.e., the channel has one fixed point

For the case of r=1 and q=2, i.e., the channel has one fixed point and one metastable point, forming a one-dimensional MM with the EMSs<sup>23</sup>

$$|\rho_{\text{FMS}}^{1,2}\rangle\rangle = |\rho_{\text{fix}}\rangle\rangle + c_2^{M,m}|R_2\rangle\rangle/h, \tag{10}$$

where  $c_2^M$  ( $c_2^m$ ) is the maximal (minimal) eigenvalue of  $L_2$ , and  $h = \sqrt{\langle \langle L_2 | L_2 \rangle \rangle \langle \langle R_2 | R_2 \rangle \rangle}$  is a normalization coefficient.

#### Metastability in sequential RIMs

The dynamics of the bath system after a RIM sequence of the probe is described by a quantum channel, which can be represented in the Stinespring representation as

$$\Phi(\rho_n) = \operatorname{Tr}_{e}[U(\rho_e \otimes \rho_n)U^{\dagger}] \tag{11}$$

where  $\rho_e = R_{\phi_1}(\frac{\pi}{2})|0\rangle_e \langle 0|R_{\phi_1}^{\dagger}(\frac{\pi}{2})$ . For the Hamiltonian

$$H = \sigma_e^z \otimes B_n + \mathbb{I}_e \otimes C_n, \tag{12}$$

the unitary evolution can be decomposed as  $U=e^{-iH\tau}=\sum_{\alpha=0,1}|\alpha\rangle_e\langle\alpha|\otimes U_\alpha$  with  $U_\alpha=e^{-i(-1)^\alpha B_n+C_n)\tau}$ . After partially tracing over the probe, the channel can be transformed to the Kraus representation as

$$\Phi(\rho_n) = \sum_{a=0,1} \mathcal{M}_a(\rho_n) = \sum_{a=0,1} M_a \rho_n M_a^{\dagger}, \tag{13}$$

where  $\mathcal{M}_a(\cdot) = M_a(\cdot)M_a^{\dagger}$  is a superoperator with the Kraus operator  $M_a = [U_0 - (-1)^a e^{i\Delta\phi} U_1]/2$  and  $\Delta\phi = \phi_1 - \phi_2$  is the phase difference between the rotation axes of  $R_{\phi_1}(\frac{\pi}{2})$  and  $R_{\phi_2}(\frac{\pi}{2})$ . Then, the natural representation of the channel for the RIM case is

$$\hat{\Phi} = \hat{\mathcal{M}}_0 + \hat{\mathcal{M}}_1 = (\hat{\mathcal{U}}_0 + \hat{\mathcal{U}}_1)/2, \tag{14}$$

where  $\hat{\mathcal{M}}_a = M_a \otimes M_a^*$  and  $\hat{\mathcal{U}}_\alpha = U_\alpha \otimes U_\alpha^*$ .

It has been proved that the spectrum of the quantum channel induced by RIM is determined by the commutativity of  $B_n$  and  $C_n^{23}$ . If

 $[B_n, C_n] = 0$ , then  $B_n$  and  $C_n$  can be diagonalized simultaneously

$$B_n = \sum_{k=1}^d b_k |k\rangle\langle k|, \quad C_n = \sum_{k=1}^d h_k |k\rangle\langle k|.$$
 (15)

The fixed points are spanned by all the rank-1 projectors  $\{|k\rangle\langle k|\}_{k=1}^d$ . While if  $[B_n, C_n] \neq 0$ ,  $B_n$  and  $C_n$  can only be block diagonalized with a unitary transformation,

$$B_n = W\left(\bigoplus_{i=1}^r B_{n,i}\right) W^{\dagger}, \quad C_n = W\left(\bigoplus_{i=1}^r C_{n,i}\right) W^{\dagger}$$
 (16)

where r (<d) is the number of blocks. Such a block diagonalization partitions the Hilbert space of the bath system into a direct sum of r subspaces  $\mathcal{H} = \bigoplus_{j=1}^r \mathcal{H}_j$ . Then it can be proved that the fixed points in this case are spanned by all the projectors  $\{\Pi_j\}_{j=1}^r$  to the blocks.

Moreover, it has also been demonstrated that when  $C_n$  is a perturbation of  $B_n$ , i.e.,  $||C_n||/||B_n||$  is small with  $||\cdot||$  denoting the operator norm, the EMSs are approximately the eigenstates of  $B_n^{23}$ .

# Model for the NV system

The full Hamiltonian for the system containing the NV electron and the  $^{14}{\rm N}$  nuclear spin is

$$H = DS_{r}^{2} + \gamma_{o} \mathbf{B} \cdot \mathbf{S} + \mathbf{S} \cdot \mathbf{A} \cdot \mathbf{I} + QI_{r}^{2} + \gamma_{o} \mathbf{B} \cdot \mathbf{I}, \tag{17}$$

where  $\mathbb{A}$  is the hyperfine interaction tensor, containing only the *zz*-component  $A_{zz}S_Jz$  and the transverse component  $A_{\perp}(S_xJ_x+S_yJ_y)$  for the <sup>14</sup>N nuclear spin. Since the large zero-field splitting of the NV electron spin suppresses the transition between  $|m_s=0\rangle$  and  $|m_s=\pm 1\rangle$ , the Hamiltonian Eq. (17) can be well approximated as a pure-dephasing form in Eq. (1) under the second-order perturbation<sup>54</sup>.

Let  $H_0 = DS_z^2 - \gamma_e B_z S_z + S_z A_{zz} I_z + Q I_z^2 - \gamma_n \mathbf{B} \cdot \mathbf{I}$  and  $H_1 = -\gamma_e (B_x S_x + B_y S_y) + A_\perp (S_x I_x + S_y I_y)$ , then  $H_1$  is a perturbation on  $H_0$ . The second-order perturbation gives  $\tilde{H}_1 = \sum_{\alpha} |\alpha\rangle_e |\alpha| \otimes H_{\alpha}^{\alpha}$ , in which

$$H_n^{\alpha} = P_{\alpha}^{e} H_1 \frac{1}{E_{\alpha} - (\mathbb{I}_{e} - P_{\alpha}^{e}) H_0(\mathbb{I}_{e} - P_{\alpha}^{e})} H_1 P_{\alpha}^{e}, \tag{18}$$

with  $E_{\alpha} = D\alpha^2 - \gamma_e B_z \alpha$ . Specifically, we have

$$H_n^{\alpha} \approx \frac{\gamma_e(2-3|\alpha|)}{2D} \left[ -\gamma_e \left( B_x^2 + B_y^2 \right) + 2A_{\perp} \left( B_x I_x + B_y I_y \right) \right]. \tag{19}$$

In the rotating frame associated with  $H_R = DS_z^2 + \gamma_e B_z S_z$ , the Hamiltonian becomes

$$H = e^{iH_R t} (H - H_R) e^{-iH_R t}$$

$$= A_{zz} S_z I_z + Q I_z^2 - \gamma_n \mathbf{B} \cdot \mathbf{I} + \tilde{H}_1,$$
(20)

which is time-independent since  $[H_R, \tilde{H}_1] = 0$  under the second-order perturbation. The above equation can be cast in the form of Eq. (12) with  $B_n = A_{zz}I_z$  and  $C_n = QI_z^2 - \gamma_n \mathbf{B} \cdot \mathbf{I} + \tilde{H}_1$ .

When the magnetic field is perfectly aligned along the NV axis,  $[B_n, C_n] = 0$ , the fixed points of the channel are  $P_{\beta}^n = |\beta\rangle_n \langle \beta|$ , with  $\beta = 0$ ,  $\pm 1$ . But when the magnetic field deviates slightly from the axis,  $[B_n, C_n] \neq 0$ , the channel has only one fixed point, which is the maximum mixed state  $\mathbb{I}_n/3 = (P_1^n + P_0^n + P_{-1}^n)/3$ , and two metastable points. The convex combination of the fixed point and the two metastable points spans a two-dimensional MM holding three EMSs, which are approximately  $P_{\beta}^n$ . We note that the eigenvalues  $\lambda_2$  and  $\lambda_3$  of two metastable points with eigenvalues are usually different  $(|\lambda_2| > |\lambda_3|)$ , which makes it difficult to directly observe the three-peak feature in experiments.

As m is so large that the contribution of one metastable point can be neglected ( $|\lambda_3|^m \to 0$ ), the remaining metastable point, together with

the fixed point, span a one-dimensional MM with two EMSs, which can be calculated by Eq. (10). For Fig. 2, numerical calculations show that the two observed EMSs are  $\rho_{\rm D}=P_1^n$  and  $\rho_{\rm B}=(P_0^n+P_{-1}^n)/2$ .

#### Model for the optical readout process

In this section, we model the optical readout process of NV centers at room temperature. In the readout process, we use a green laser to excite the NV electron and collect the emitted photons. The NV electron spin in state  $|\pm 1\rangle_e$  has a greater chance to relax to the singlet state (via inter-system crossing), resulting in a lower photon number in the detection window (650–800 nm). This provides a convenient and efficient mechanism to distinguish the NV spin states by the "bright-dark" contrast, corresponding to the  $|0\rangle_e$  and  $|\pm 1\rangle_e$  states, respectively.

The optical readout process corresponds to a non-selective projective measurement of the NV electron spin, and can be modeled as a series of Kraus operators  $\{K_n\}_{n=0}^{\infty}$ . If n photons are collected by the counter, the Kraus operator  $K_n$  acting on the NV electron spin is<sup>55</sup>

$$K_n = \sum_{\alpha = 0, 1} \sqrt{p(n|\alpha)} P_{\alpha}^e, \tag{21}$$

where  $P_{\alpha}^{e}$  is projector on subspace  $\alpha$  and collected photon numbers obey Poisson distribution  $p(n|\alpha) = \frac{1}{n!}e^{-n_{\alpha}}n_{\alpha}^{n}$  with  $n_{\alpha}$  being the average photon number obtained for state  $|\alpha\rangle_{n}$ . If  $n_{\alpha}$  is small (about 0.05 in our experiments), truncating to  $K_{0}$  and  $K_{1}$  is a good approximation with  $p(1|\alpha) = n_{\alpha}$  and  $p(0|\alpha) = 1 - p(1|\alpha)$ .

Then, the Kraus operator on the  $^{14}N$  bath spin when obtaining n photons can be derived as

$$W_{n}(\rho) = \operatorname{Tr}_{e}\{K_{n}\mathcal{P}[R_{\phi_{2}}UR_{\phi_{1}}(|0\rangle_{e}\langle 0|\otimes \rho)R_{\phi_{1}}^{\dagger}U^{\dagger}R_{\phi_{2}}^{\dagger}]K_{n}^{\dagger}\}$$

$$= \sum_{\alpha=0}^{\infty} p(n|\alpha)M_{\alpha}\rho M_{\alpha}^{\dagger},$$
(22)

where  $\mathcal{P}(\cdot) = \sum_{\alpha=0,1} P_{\alpha}^{e}(\cdot) P_{\alpha}^{e}$  is the channel for non-selective projective measurement of the electron spin, and  $M_{\alpha} = [U_{0} - (-1)^{\alpha} e^{i\Delta\phi} U_{1}]$  is the Kraus operator introduced in Eq. (2) for the nuclear spin. Note that

$$\hat{\Phi}' = \sum_{n} \hat{W}_{n} = \sum_{\alpha=0,1} \sum_{n} p(n|\alpha) \hat{M}_{\alpha} = \hat{\Phi}, \tag{23}$$

then the channel with the set of Kraus operators  $\{W_n\}_{n=0}^{\infty}$  is the same as that with  $\{M_{\alpha}\}_{\alpha=0,1}$ , so the analysis of the channel decomposition in the section above also applies here.

#### Measurement statistics of sequential RIMs

The fixed points (or metastable points) can be observed by the measurement statistics of sequential RIMs. A single RIM on the probe spin has an outcome  $a \in \{0, 1\}$ , and for sequential RIMs we obtain a sequence of binary numbers  $\{a_1, \cdots, a_m\}$ . This sequence of measurement outcomes defines a quantum trajectory. We then look for some statistical observable that can characterize different quantum trajectories and their corresponding fixed points.

In practice, we often focus on the average of the m measurement results and its expectation, i.e.,  $\bar{a} = \frac{1}{m} \sum_{n=1}^{m} a_n$ , which in our case coincides with the measurement frequency  $f_1 = m_0/m$  and can be related to the measurement polarization by  $X = 1/2 - f_1$ . The expectation of  $f_1$  can be written as

$$\langle f_1 \rangle = \sum_{a_1} \cdots \sum_{a_m} f_1 p(a_1, \cdots, a_m | \rho), \tag{24}$$

where the probability to get a specific sequence of measurement results  $\{a_1, \dots, a_m\}$  is given by

$$p(a_1, \dots, a_m | \rho) = \langle \langle \mathbb{I} | \hat{\mathcal{M}}_{a_m} \dots \hat{\mathcal{M}}_{a_1} | \rho \rangle \rangle. \tag{25}$$

It can be shown that in the asymptotic limit, i.e., when the number of repetitions is large enough  $m \to \infty$ ,  $\langle f_1 \rangle$  is only determined by fixed points<sup>24</sup>,

$$\lim_{m \to \infty} \langle f_1 \rangle = \sum_{j=1}^{J} c_j \langle f_{1j} \rangle_*, \tag{26}$$

where we assume there are J fixed points with

$$\langle f_{1i} \rangle_* = \langle \langle \mathbb{I} | \hat{\mathcal{M}}_1 | \rho_{\text{fiv}}^j \rangle \rangle = p(1|\rho_{\text{fiv}}^j),$$
 (27)

with  $c_j = {\rm Tr}\,(\rho_{\rm fix}^j \rho)$  being the probability of obtaining the j-th fixed point given the initial state  $\rho$ . Note that the above equation indicates that the expectation of the measurement average coincides with the probability of obtaining result a=1 for the fixed point  $\rho_{\rm fix}^j$  in a single RIM,

$$p(a|\rho) = \text{Tr}(M_a \rho M_a^{\dagger}) = \langle \langle \mathbb{I} | \hat{\mathcal{M}}_a | \rho \rangle \rangle. \tag{28}$$

In other words, the distribution of the measured frequency  $f_1$  can have J peaks, centering around the set of expectations  $\{\langle f_{1j}\rangle_*\}_{j=1}^J$ . Each peak includes all the trajectories with  $f_1$  close to  $\langle f_{1j}\rangle_*^{34}$ .

Taking into account the optical readout process, the average photon number corresponding to the *j*th fixed (metastable) point is

$$\langle n_j \rangle_* = \sum_n \langle \langle \mathbb{I} | n \hat{\mathcal{W}}_n | \rho_{\text{fix}}^j \rangle \rangle$$
  
= 
$$\sum_{n,\alpha} n p(n|\alpha) \langle f_{\alpha j} \rangle_*$$
 (29)

where  $\hat{W}_n = W_n \otimes W_n^* = \sum_{\alpha=0,1} p(n|\alpha) \hat{\mathcal{M}}_{\alpha}$  is the superoperator of  $W_n$  in the HS space.

#### Data availability

The data generated in this study are provided in the Source Data file. Source data are provided with this paper.

## **Code availability**

The codes used for the current study are available on request from the corresponding author.

# References

- Mori, T., Ikeda, T. N., Kaminishi, E. & Ueda, M. Thermalization and prethermalization in isolated quantum systems: a theoretical overview. J. Phys. B 51, 112001 (2018).
- Hodgman, S. S. et al. Metastable helium: a new determination of the longest atomic excited-state lifetime. *Phys. Rev. Lett.* 103, 053002 (2009).
- Balan, A. et al. Direct observation of magnetic metastability in individual iron nanoparticles. Phys. Rev. Lett. 112, 107201 (2014).
- Karube, K. et al. Robust metastable skyrmions and their triangular–square lattice structural transition in a high-temperature chiral magnet. *Nat. Mater.* 15, 1237 (2016).
- Han, T.-R. T. et al. Exploration of metastability and hidden phases in correlated electron crystals visualized by femtosecond optical doping and electron crystallography. Sci. Adv. 1, e1400173 (2015).
- Macieszczak, K., Guţă, M., Lesanovsky, I. & Garrahan, J. P. Towards a theory of metastability in open quantum dynamics. *Phys. Rev. Lett.* 116, 240404 (2016).
- Macieszczak, K., Rose, D. C., Lesanovsky, I. & Garrahan, J. P. Theory of classical metastability in open quantum systems. *Phys. Rev. Res.* 3, 033047 (2021).

- Brown, C. A., Macieszczak, K. & Jack, R. L. Unraveling metastable Markovian open quantum systems. *Phys. Rev. A* 109, 022244 (2024).
- Rose, D. C., Macieszczak, K., Lesanovsky, I. & Garrahan, J. P. Metastability in an open quantum Ising model. *Phys. Rev. E* 94, 052132 (2016).
- Le Boité, A., Hwang, M.-J. & Plenio, M. B. Metastability in the drivendissipative Rabi model. *Phys. Rev. A* 95, 023829 (2017).
- Gong, Z., Hamazaki, R. & Ueda, M. Discrete time-crystalline order in cavity and circuit QED systems. *Phys. Rev. Lett.* 120, 040404 (2018).
- Gambetta, F. M., Carollo, F., Marcuzzi, M., Garrahan, J. P. & Lesanovsky, I. Discrete time crystals in the absence of manifest symmetries or disorder in open quantum systems. *Phys. Rev. Lett.* 122, 015701 (2019).
- Landa, H., Schiró, M. & Misguich, G. Multistability of drivendissipative quantum spins. *Phys. Rev. Lett.* 124, 043601 (2020).
- Flynn, V. P., Cobanera, E. & Viola, L. Topology by dissipation: Majorana bosons in metastable quadratic Markovian dynamics. *Phys. Rev. Lett.* 127, 245701 (2021).
- Defenu, N. Metastability and discrete spectrum of long-range systems. Proc. Natl. Acad. Sci. USA 118, e2101785118 (2021).
- Jäger, S. B., Schmit, T., Morigi, G., Holland, M. J. & Betzholz, R. Lindblad master equations for quantum systems coupled to dissipative bosonic modes. *Phys. Rev. Lett.* 129, 063601 (2022).
- Cabot, A., Carollo, F. & Lesanovsky, I. Metastable discrete timecrystal resonances in a dissipative central spin system. *Phys. Rev. B* 106, 134311 (2022).
- Blume-Kohout, R., Ng, H. K., Poulin, D. & Viola, L. Characterizing the structure of preserved information in quantum processes. *Phys. Rev. Lett.* 100, 030501 (2008).
- Blume-Kohout, R., Ng, H. K., Poulin, D. & Viola, L. Informationpreserving structures: a general framework for quantum zero-error information. *Phys. Rev. A* 82, 062306 (2010).
- Fitzpatrick, M., Sundaresan, N. M., Li, A. C. Y., Koch, J. & Houck, A. A. Observation of a dissipative phase transition in a one-dimensional circuit QED lattice. *Phys. Rev. X* 7, 011016 (2017).
- Letscher, F., Thomas, O., Niederprüm, T., Fleischhauer, M. & Ott, H. Bistability versus metastability in driven dissipative Rydberg gases. *Phys. Rev. X* 7, 021020 (2017).
- Beaulieu, G. et al. Observation of first-and second-order dissipative phase transitions in a two-photon driven Kerr resonator. *Nat. Commun.* 16, 1954 (2025).
- Jin, Y.-D., Qiu, C.-D. & Ma, W.-L. Theory of metastability in discretetime open quantum dynamics. *Phys. Rev. A* 109, 042204 (2024).
- Qiu, C.-D., Jin, Y.-D., Zhang, J.-X., Liu, G.-Q. & Ma, W.-L. How coherence measurements of a qubit steer its quantum environment. *Phys. Rev. B* 110, 024311 (2024).
- 25. Watrous, J. The Theory of Quantum Information (Cambridge University Press, 2018).
- Gudder, S. Quantum Markov chains. J. Math. Phys. 49, 072105 (2008).
- 27. Amato, D., Facchi, P. & Konderak, A. Asymptotics of quantum channels. J. Phys. A **56**, 265304 (2023).
- 28. Ramsey, N. F. A molecular beam resonance method with separated oscillating fields. *Phys. Rev.* **78**, 695 (1950).
- Lee, H., Kok, P. & Dowling, J. P. A quantum Rosetta stone for interferometry. J. Mod. Opt. 49, 2325 (2002).
- 30. Degen, C. L., Reinhard, F. & Cappellaro, P. Quantum sensing. *Rev. Mod. Phys.* **89**, 035002 (2017).
- 31. Arias, A., Gheondea, A. & Gudder, S. Fixed points of quantum operations. *J. Math. Phys.* **43**, 5872 (2002).
- Albert, V. V. Asymptotics of quantum channels: conserved quantities, an adiabatic limit, and matrix product states. Quantum 3, 151 (2019).
- Bauer, M. & Bernard, D. Convergence of repeated quantum nondemolition measurements and wave-function collapse. *Phys. Rev. A* 84, 044103 (2011).

- 34. Ma, W.-L., Li, S.-S. & Liu, R.-B. Sequential generalized measurements: asymptotics, typicality, and emergent projective measurements. *Phys. Rev. A* **107**, 012217 (2023).
- Wang, P., Yang, W. & Liu, R. Using weak measurements to synthesize projective measurement of nonconserved observables of weakly coupled nuclear spins. *Phys. Rev. Appl.* 19, 054037 (2023).
- Dréau, A., Spinicelli, P., Maze, J. R., Roch, J.-F. & Jacques, V. Singleshot readout of multiple nuclear spin qubits in diamond under ambient conditions. *Phys. Rev. Lett.* 110, 060502 (2013).
- 37. Neumann, P. et al. Single-shot readout of a single nuclear spin. *Science* **329**, 542 (2010).
- 38. Maurer, P. C. et al. Room-temperature quantum bit memory exceeding one second. *Science* **336**, 1283 (2012).
- Ma, W.-L., Wang, P., Leong, W.-H. & Liu, R.-B. Phase transitions in sequential weak measurements. Phys. Rev. A 98, 012117 (2018).
- Bernien, H. et al. Heralded entanglement between solid-state qubits separated by three metres. *Nature* 497, 86 (2013).
- 41. Cai, J. et al. A large-scale quantum simulator on a diamond surface at room temperature. *Nat. Phys.* **9**, 168 (2013).
- 42. Abobeih, M. H. et al. Fault-tolerant operation of a logical qubit in a diamond quantum processor. *Nature* **606**, 884 (2022).
- Randall, J. et al. Many-body-localized discrete time crystal with a programmable spin-based quantum simulator. Science 374, 1474 (2021).
- 44. Soshenko, V. V. et al. Nuclear spin gyroscope based on the nitrogen vacancy center in diamond. *Phys. Rev. Lett.* **126**, 197702 (2021).
- Blok, M. et al. Manipulating a qubit through the backaction of sequential partial measurements and real-time feedback. *Nat. Phys.* 10, 189 (2014).
- Bonato, C. et al. Optimized quantum sensing with a single electron spin using real-time adaptive measurements. *Nat. Nano.* 11, 247 (2016).
- Burrell, A. H., Szwer, D. J., Webster, S. C. & Lucas, D. M. Scalable simultaneous multiqubit readout with 99.99% single-shot fidelity. *Phys. Rev. A* 81, 040302 (2010).
- Pfender, M. et al. High-resolution spectroscopy of single nuclear spins via sequential weak measurements. *Nat. Commun.* 10, 594 (2019).
- Taminiau, T. et al. Detection and control of individual nuclear spins using a weakly coupled electron spin. *Phys. Rev. Lett.* 109, 137602 (2012).
- 50. Taylor, J. M. et al. High-sensitivity diamond magnetometer with nanoscale resolution. *Nat. Phys.* **4**, 810 (2008).
- 51. Sadzak, N. et al. A Hahn-Ramsey scheme for dynamical decoupling of single solid-state qubits. *Front. Photonics* **3**, 932944 (2022).
- Wang, Y.-X. & Clerk, A. A. Intrinsic and induced quantum quenches for enhancing qubit-based quantum noise spectroscopy. *Nat. Commun.* 12, 6528 (2021).
- 53. Jerger, P. C. et al. Detecting spin-bath polarization with quantum quench phase shifts of single spins in diamond. *PRX Quantum* **4**, 040315 (2023).
- 54. Childress, L. et al. Coherent dynamics of coupled electron and nuclear spin qubits in diamond. Science **314**, 281 (2006).
- 55. Meinel, J. et al. Quantum nonlinear spectroscopy of single nuclear spins. *Nat. Commun.* **13**, 5318 (2022).

# **Acknowledgements**

This work is supported by the Innovation Program for Quantum Science and Technology (Grants Nos. 2023ZD0300600, 2021ZD0302300), the National Key Research and Development Program of China (Grants No. 2023YFA1608900), the National Natural Science Foundation of China (Grant Nos. 12022509, 11934018, T2121001), and the Chinese Academy of Sciences (Grant Nos. YSBR90, YSBR-100, EOSEBB11, E27RBB11).

# **Author contributions**

W.L.M. and G.Q.L. conceived the project. J.X.Z. conducted the experiments with the supervision of G.Q.L. and Y.D.J. C.D.Q. performed theoretical analysis and simulations with the supervision of W.L.M. All authors contributed to the writing of the paper.

# **Competing interests**

The authors declare no competing interests.

# **Additional information**

**Supplementary information** The online version contains supplementary material available at https://doi.org/10.1038/s41467-025-64772-6.

**Correspondence** and requests for materials should be addressed to Wen-Long Ma or Gang-Qin Liu.

**Peer review information** *Nature Communications* thanks the anonymous reviewers for their contribution to the peer review of this work. A peer review file is available.

**Reprints and permissions information** is available at http://www.nature.com/reprints

**Publisher's Note** Springer Nature remains neutral with regard to jurisdictional claims in published maps and institutional affiliations.

Open Access This article is licensed under a Creative Commons Attribution-NonCommercial-NoDerivatives 4.0 International License, which permits any non-commercial use, sharing, distribution and reproduction in any medium or format, as long as you give appropriate credit to the original author(s) and the source, provide a link to the Creative Commons licence, and indicate if you modified the licensed material. You do not have permission under this licence to share adapted material derived from this article or parts of it. The images or other third party material in this article are included in the article's Creative Commons licence, unless indicated otherwise in a credit line to the material. If material is not included in the article's Creative Commons licence and your intended use is not permitted by statutory regulation or exceeds the permitted use, you will need to obtain permission directly from the copyright holder. To view a copy of this licence, visit <a href="https://creativecommons.org/licenses/by-nc-nd/4.0/">https://creativecommons.org/licenses/by-nc-nd/4.0/</a>.

© The Author(s) 2025